Water Research 188 (2021) 116529

Contents lists available at ScienceDirect

Water Research

journal homepage: www.elsevier.com/locate/watres

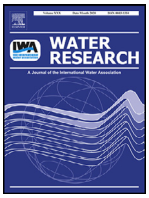

Metal-free black-red phosphorus as an efficient heterogeneous reductant to boost Fe^{3+}/Fe^{2+} cycle for peroxymonosulfate activation

Hongyu Zhou[a,b], Jiali Peng[a,b], Jiayi Li[a,b], Junjie You[a,b], Leiduo Lai[a,b], Rui Liu[c], Zhimin Ao[d], Gang Yao[b,e], Bo Lai[a,b,*]

[a] *State Key Laboratory of Hydraulics and Mountain River Engineering, College of Architecture and Environment, Sichuan University, Chengdu 610065, China*
[b] *Sino-German Centre for Water and Health Research, Sichuan University, Chengdu 610065, China*
[c] *State Key Laboratory of Environmental Chemistry and Ecotoxicology, Research Center for Eco-Environmental Sciences, Chinese Academy of Sciences, Beijing 100085, China*
[d] *Guangdong Key Laboratory of Environmental Catalysis and Health Risk Control, Institute of Environmental Health and Pollution Control, School of Environmental Science and Engineering, Guangdong University of Technology, Guangzhou 51006, China*
[e] *Institute of Environmental Engineering, RWTH Aachen University, Germany*

ARTICLE INFO

Article history:
Received 17 August 2020
Revised 9 October 2020
Accepted 16 October 2020
Available online 17 October 2020

Keywords:
Black-red phosphorus
Peroxymonosulfate
Fe^{3+}/Fe^{2+} cycle
Mechanism

ABSTRACT

In this work, a novel metal-free black-red phosphorus (BRP) was prepared from red phosphorus (RP) and applied in Fe^{2+}/peroxymonosulfate (PMS) process. Compared with that of RP, the contaminant degradation performance of BRP was significantly elevated due to the enhanced electron transfer from BRP to Fe^{3+}. This enhancement was mainly induced by size decrease effect, the removal of oxidation layer and the partial phase conversion. Moreoevr, BRP avoided the radical quenching reaction caused by reductant itself, whereas it was inevitable using homogeneous reductant like hydroxylamine. More importantly, the system had a superior recyclability and strong resistance to natural water. Though concurrent side-reaction between PMS and BRP occured, multiple PMS dosage could remarkedly alleviated the side-reaction, thus elevating PMS utilization efficiency. The dominant BRP oxidation products included phosphite and phosphate. Interestingly, moderate increase of Fe^{3+} concentration could efficiently reduce the by-product formation via the prompt PMS activation by regenerated Fe^{2+}. Our work clarified the acceleration mechanism of Fe^{3+}/Fe^{2+} cycle by BRP and proposed the control strategy of by-prodoct formation.

1. Introduction

Fe^{2+}-activated H_2O_2, peroxymonosulfate (PMS) and peroxydisulfate (PDS) advanced oxidation processes Eqs. (1)–((3), (Pignatello et al., 2006; Xiao et al., 2020)) have been intensively investigated for decades of years due to their high oxidation capacity and low environmental toxicity (Anipsitakis and Dionysiou, 2004; Rastogi et al., 2009). However, the rate-limiting regeneration of Fe^{2+} from Fe^{3+} heavily hampers the successive activation of these peroxides, which is generally considered as the Achille's heels in Fe-based peroxide activation reactions (Pignatello et al., 2006). Besides, excessive Fe^{2+} dosage might also result in secondary iron sludge pollution (Zhang et al., 2019a). Therefore, accelerating Fe^{3+}/Fe^{2+} cycle has become one of the most intractable issues for their application. To date, many efforts have been made to overcome this bottleneck like the introduction of electric field (Brillas et al., 2009), UV/Vis light (Andreozzi et al., 2006; Wang et al., 2007) and reducing agents (Fukuchi et al., 2014; Xing et al., 2018). Especially, the introduction of reducing agents like homogeneous hydroxylamine (Li et al., 2019) and cysteine (Li et al., 2016) as well as heterogeneous metal sulfides (Liu et al., 2018a) has been broadly studied due to their strong reducibility and operating simplicity. Nevertheless, some intrinsic drawbacks are still hard to overcome like the toxicity and non-recyclability of hydroxylamine, the extra total organic carbon of cysteine and the secondary pollution of heavy metal dissolution.

$$Fe^{2+} + H_2O_2 \rightarrow Fe^{3+} + \bullet OH + OH^- \quad k = 76\ M^{-1}\cdot s^{-1} \tag{1}$$

$$Fe^{2+} + HSO_5^- \rightarrow Fe^{3+} + SO_4^{\bullet-} + OH^- \quad k = 3 \times 10^4\ M^{-1}\cdot s^{-1} \tag{2}$$

$$Fe^{2+} + S_2O_8^{2-} \rightarrow Fe^{3+} + SO_4^{\bullet-} + SO_4^{2-} \quad k = 3 \times 10^1\ M^{-1}\cdot s^{-1} \tag{3}$$

---

[*] Corresponding author.
E-mail address: laibo1981@163.com (B. Lai).

https://doi.org/10.1016/j.watres.2020.116529
0043-1354/

Compared with the metal-bearing reductants, non-metallic element like boron, carbon, sulfur and phosphorus and their oxyacid anions are usually possessed with lower toxicity. The final oxidation products like carbonate, sulfate and phosphate are also ubiquitous in the natural matrix. Moreover, previous studies have also pointed out the excellent physicochemical properties of these non-metallic elements. For instance, in environmental remediation, non-metallic elements have been previously investigated such as organic adsorption by multi-wall carbon nanotube (MWCNT) (Apul and Karanfil, 2015) and photocatalytic bacteria inactivation by red phosphorus (RP) (Xia et al., 2015). Recently, Duan et al. (2019) also found that non-metallic boron and black phosphorus (BP) could directly activate PMS to produce hydroxyl radicals (•OH) and sulfate radicals ($SO_4^{\bullet -}$), indicating the strong electron-donating ability of these non-metallic elements. However, the direct activation performance seemed inferior and the recyclability was unsatisfactory. Similarly, in our previous work, we also found that MoS_2 could directly activate PMS and PDS but the re-utilization efficiency gradually declined after several runs (Zhou et al., 2020). Of note, it was reported that the addition of Fe^{3+} in MoS_2/PMS (Sheng et al., 2019), MoS_2/PDS (He et al., 2020) and MoS_2/H_2O_2 (Xing et al., 2018) systems could significantly promote the decomposition of peroxides and accelerate target contaminant degradation. Inspired by these facts, we expect that the combination of electron-rich non-metallic elements, Fe^{3+} and different peroxides could also boost radical generation and expedite contaminant degradation.

Herein, in this work, we first studied the potential of different non-metallic elements (i.e., amorphous boron, MWCNT, RP, silica, sulfur and selenium) in promoting Fe^{3+}/Fe^{2+} cycle for PMS activation. Carbamazepine (CBZ) was selected as the target contaminant due to its potential threat to aquatic lives (Soufan et al., 2013). Then, we dominantly investigate the performance of RP due to its moderate performance and low cost. Furthermore, we modified RP into hydrothermal red phosphorus (HRP) and black-red phosphorus (BRP) to enhance its reducibility. The performance of HRP and BRP was evaluated and the crucial factors that enhanced the reducibility of pristine RP were discerned. The practical application performance in actual water and influence of water parameters like pH and dissolved O_2 were also investigated. Besides, the reaction kinetics and the effects of multiple dosage modes on CBZ degradation were in detail discussed. Moreover, the generation and transformation of intermediate phosphorus anions were monitored and the chemisorption of PMS was simulated via density functional theory (DFT) calculation. Based on experimental and theoretical results, the reaction mechanism among Fe^{3+}, PMS and BRP was elucidated. Finally, the control strategies of phosphorus by-product generation were also proposed.

2. Materials and methods

2.1. Materials

The details of materials were listed in Text S1.

2.2. Experimental procedure

2.2.1. BRP synthesis

BRP was synthesized using an ethylenediamine (EDA) method (Liu et al., 2019). First, 1.5 g commercial RP and 60 mL deionized water were added in 100 mL stainless Teflon-lined autoclave and sealed at 200°C for 12 h to obtain HRP. Then the HRP was washed with deionized water and ethanol 3 times respectively and dried at 50°C in vacuum overnight. Next, 1.0 g HRP and 60 mL EDA were simultaneously added into 100 mL stainless Teflon-lined autoclave and sealed at 140°C for 12 h. After cooling down, the black products were washed with deoxygenated water and ethanol 3 times respectively and then dried at 50°C in vacuum overnight. The obtained powder was thoroughly ground and then sifted through a 200 mesh sieve.

2.2.2. Degradation procedures

For contaminant degradation experiments, all bath experiments were conducted in 250 mL beaker containing 150 mL contaminant solution. The temperature was kept at 30 ± 1°C by water batch heating. The pH of the solution was adjusted with 0.1 M H_2SO_4 and 0.1 M NaOH, if necessary. The stock solution of contaminants was diluted into the working concentration and then certain amount of PMS stock solution, Fe^{3+}/Fe^{2+} stock solution and materials were added successively to initiate the reaction. At the predetermined time, 1.5 mL samples were taken, mixed with 20 μL ethanol (EtOH) and quickly filtered through a 0.22 μm PTFE syringe filter discs for the analysis of residual contaminant concentration. For Cr (VI) removal experiment, the experimental prodedures were similar to the above except that no Fe^{3+} and EtOH were added and the sample volume was 3 mL.

2.3. Characterization

The morphologi**e**s of RP, HRP and BRP were investigated using scanning electron microscope (SEM, SU8010, Hitachi, Japan). Transmission electron microscope (TEM) was conducted on FEI Tecnai G2 F20 S-TWIN at a voltage of 200 V (Hillsboro, Oregon, USA). High-resolution transmission electron microscope (HRTEM) was conducted on JEOL, cat. no. JEM-2100F. Raman spectra were recorded using a HORIBA LabRAM HR spectrometer with a 532 nm excitation laser. Fourier transform infrared spectroscopy (FT-IR) was conducted on Nicolet is50 (Thermo Fisher). X-ray diffraction (XRD) patterns were acquired using PANalytical B.V with a scan rate of 2°/min (Holland). The specific surface areas of RP, HRP and BRP were measured based on the Brunauer-Emmett-Teller (BET) method using a surface area and porosity analyzer (TriStar II 3020, Micromeritics, Norcross, GA). The surface chemical oxidation states were recorded by an X-ray photoelectron spectroscopy (XPS, AXIS Ultra DLD, Kratos Co., UK). Electron paramagnetic resonance (EPR) signals were recorded using DMPO as a spin-trapping agent on Bruker EMX plus X-band CW EPR spectrometer. EPR detection conditions were microwave frequency: 9.83 GHz; microwave power: 2.00 mW. Nyquist plots and Tafel scans were acquired on CHI 604E electrochemical workstation (Chenhua Instrument, shanghai, China) with glassy carbon electrode as the working electrode, platinum wire as the counter electrode and Ag/AgCl electrode as the reference electrode.

2.4. Analytic methods

The concentration of target organics was measured using high performance liquid chromatography (HPLC, LC-16, SHIMAZU) equipped with a InertSustain C18 separation column (4.6 × 250 mm). The detailed HPLC condition is listed in Table S1. The concentration of hypophosphite ($H_2PO_2^-$), phosphite (H_3PO_3), phosphate ($H_2PO_4^-$) and pyrophosphate ($P_2O_7^{4-}$) was analyzed by Dionex AQUION ion chromatography (Thermo Fisher) using KOH as the eluent with a Dionex Ionpac^{TM} AS15 column (4×250 mm). Residual PMS concentration was analyzed using a modified ABTS method (Text S2). Fe^{2+} concentration was monitored using 1,10-phenanthroline method. Cr (VI) concentration was measured using 1,5-diphenylcarbazide method. The intermediates of CBZ were detected using UPLC-QTOF MS (Agilent 1290 infinity II UPLC with Agilent G6545 Q-TOF Mass Spectrometer) equipped with Eclipse plus-

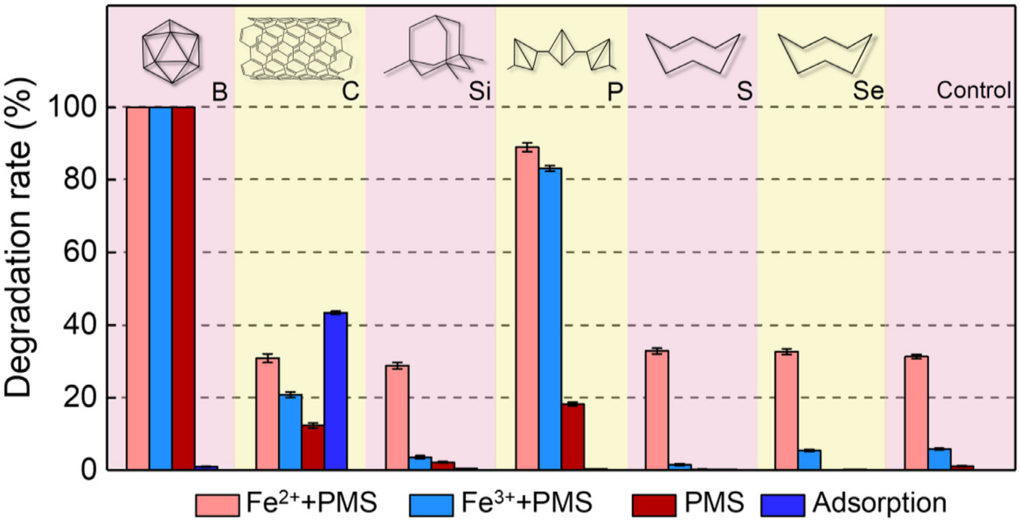

Fig. 1. The performance of different non-metallic elements in accelerating Fe^{3+}/Fe^{2+} cycle for PMS activation. Experiment conditions: [Amorphous boron] = [Silica powder] = [RP] = [Sublimed sulfur] = [Selenium powder] = 0.1 g/L, [MWCNT-OH] = 0.05 g/L, [PMS] = 0.2 mM, $[Fe^{3+}] = [Fe^{2+}]$ = 2 mg/L, $[CBZ]_0$ = 10.6 μM, pH_{ini} = 3.0, reaction time = 60 min.

C18 column (Eclipse plus-C18 3.0×100mm 1.8μm). Analysis details were provided in Text S3.

2.5. Kinetic studies and DFT calculation

The degradation of CBZ was fitted with pseudo-first-order model (Eq. (4)), where C_0 and C_t represented the CBZ concentration initially and at t moment and k_{obs} represented the apparent reaction kinetic rate. The first-principle calculation was carried out using the Vienna Ab-initio Simulation Package (VASP 5.4). The projector-augmented wave (PAW) was used to describe the electron–ion interactions, and the generalized gradient approximation functional (GGA-PBE) was applied to describe the electron exchange and correlation (Kresse and Joubert, 1999; Liu et al., 2018b). A cut-off energy of 400 eV and a k-point mesh (3 × 3 × 1) were selected (You et al., 2020). The energy and force converged to 10^{-5} eV/atom and 0.01 eV/Å, respectively. A 3 × 3 × 2 supercell of BP was established in a 15 Å vacuum gap (Cartz et al., 1979). For PMS adsorption, the adsorption energy E_{ads} was determined by Eq. (5) (Nie et al., 2020; Nie et al., 2019)

$$\ln\,(C_t/C_0) = -k_{obs} \times t \tag{4}$$

$$E_{ads} = E_{PMS/BP} - (E_{PMS} + E_{BP}) \tag{5}$$

where $E_{PMS/BP}$, E_{PMS}, and E_{BP} represented the total energies of the PMS/BP system, the isolated PMS and BP in the same slab, respectively.

3. Results and discussion

3.1. Feasibility of different non-metallic elements for Fe^{3+} reduction

To evaluate the feasibility of various non-metallic elements in promoting Fe^{3+}/Fe^{2+} cycle, we selected six typical elemental materials, including amorphous boron, hydroxyl-modified MWCNT (MWCNT-OH), silica powder, RP, sublimed sulfur and selenium, and introduced them in Fe^{2+}/PMS (or Fe^{3+}/PMS) system for CBZ degradation. As shown in Fig. 1, only 31.3% and 5.58% CBZ could be degraded in 60 min by Fe^{2+}/PMS system and Fe^{3+}/PMS system, respectively. However, with the addition of amorphous boron and RP, the CBZ degradation efficiency significantly increased to 100% and 83.2% even in Fe^{3+}/PMS system. In comparison, silica powder, sublimed sulfur and selenium powder were all ineffective for enhancing CBZ degradation.

MWCNT-OH had a superior adsorption ability towards CBZ (43.4%) while the addition of PMS and Fe^{3+} (20.81%) in turn inhibited CBZ removal. Besdies, to exclude the influence of functional groups, unfunctionalized MWCNT and carboxyl-modified MWCNT (MWCNT-COOH) were also compared and the results showed that none of them were effective for CBZ degradation (Fig. S1). This demonstrated that direct Fe^{3+} reduction by MWCNT was unfavorable. Although it was not consistent with the results of Seo et al. (2015) where MWCNT could directly reduce Fe^{3+}, the reductant dosage in their work was far more than that in this work. Fig. S2 also depicted that in the absence of PMS, amorphous boron and RP could reduce 91.5% and 28% Fe^{3+} in 60 min respectively, whereas marginal Fe^{2+} was generated by other non-metallic elemental materials. This further demonstrated the superior roles of amorphous boron and RP in PMS activation. Given the earth-abundant and cost-effective properties Tian et al., 2018; Xia et al., 2015), RP was then selected and investigated in our work. To confirm its efficiency, RP was also introduced into Fe^{3+}/H_2O_2 and Fe^{3+}/PDS systems (Fig. S3). 60.5% and 43.7% CBZ could be degraded in 60 min respectively, suggesting the efficiency followed the order of PMS > H_2O_2 > PDS. This order could be mainly ascribed to the different reaction rates between Fe^{2+} and the three peroxides (Eqs. (1)–((3)) since the initial Fe^{2+} concentration generated by RP in three systems was similar. We further replaced Fe^{3+} with different metal ions (Cu^{2+}, Ag^{+}, Ce^{3+}, Mn^{2+}, Ni^{2+}) to investigate the role of Fe^{3+} (Fig. S4). The degradation of CBZ was drastically enhanced in the presence of Cu^{2+} (83.5%), which could be due to the generation of reactive Cu^{+} (Lee et al., 2016). However, other metal ions were relatively inert to CBZ degradation, suggesting the generation of low-valence metal ions was an essential step in promoting peroxide activation.

3.2. Characterization of RP, HRP and BRP

To further enhance the reducibility of pristine RP, a facile two-step modification method was conducted to prepare HRP and BRP respectively (Liu et al., 2019). Energy-dispersive X-ray spectroscopy results showed that the pristine RP was mainly comprised of P with a part of O, which might derive from the surface oxidation

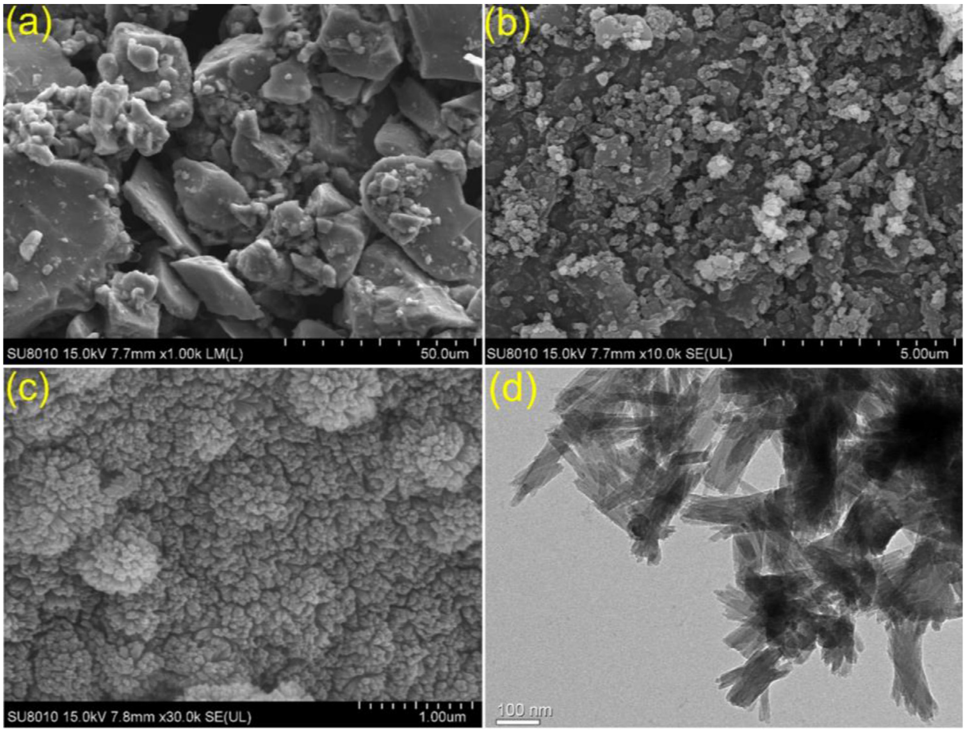

Fig. 2. SEM images of (a) pristine RP, (b) HRP and (c) BRP; (d) TEM images of BRP.

layer (Fig. S5). As shown in Fig. 2a-c, after the hydrothermal treatment, the bulk RP was split into substantial fragments and the size of pristine RP decreased from 100 μm to around 5 μm. Accordingly, the BET surface area appreciably increased from 0.1 m^2/g to 40.2 m^2/g, which would facilitate its interaction with Fe^{3+}. Subsequently, the EDA modification further transformed the fragments into flower-like spheres with some rodlike sheets sticking out. The TEM images of BRP clearly displayed an overlapped sheet structure (Fig. 2d). The BET surface area slightly declined to 16.4 m^2/g possibly due to this overlapped structure. From the HRTEM images, it could be observed that BRP was composed of both amorphous phase and crystalline phase (Fig. S6). The lattice fringes corresponded to the (0 2 0) lattice plane of BP, which confirmed the partial phase transformation after EDA modification. The digital graph also showed that the color of RP turned bright-red and further black after the two modification steps (Fig. S7).

Moreover, compared with pristine RP and HRP, three obvious peaks emerged at $2\theta = 17.3°$, 27.4° and 57.4° in the XRD patterns of BRP (Fig. 3a), which could be assigned to (0 2 0), (0 2 1) and (1 5 1) planes of BP (Antonatos et al., 2020; Shen et al., 2015). Similarly, Raman spectra also confirmed the partial conversion from RP phase to BP phase (Fig. 3b). For pristine RP, the Raman band at 346 and 393 cm^{-1} could be assigned to the fundamental mode (B_1) and symmetric stretch mode (A_1) of RP, respectively. HRP exhibited no new band compared with pristine RP. However, for BRP, apart from the bands of RP, three characteristic bands appeared at 362, 444 and 467 cm^{-1}, which could be attributed to the A_g^1 (out-of-plane mode), B_{2g} and A_g^2 (in-plane mode) of BP (Batmunkh et al., 2019).

XPS was also acquired to probe the modification-induced surface chemical state conversion. From Fig. 3c, it could be observed that N 1s peak appeared in BRP, which was induced by the EDA treatment. Nevertheless, Fig. S8 revealed that the addition of EDA could not accelerate CBZ degradation and Fe^{3+} reduction in Fe^{3+}/PMS system, which excluded the involvement of EDA in the reaction. Fig. 3d further exhibited the P 2p core-level spectra. For pristine RP, a broad peak at 134.5 eV indicated the partial surface coverage by a P_2O_5 oxidation layer, which was unfavorable for the electron transfer from RP to Fe^{3+} (Tian et al., 2018). After the hydrothermal process, the oxidation peak completely disappeared, suggesting the surface P_2O_5 dissolution. The surfacial atomic ratios of O to P from XPS results were listed in Table S2. The results also demonstrated that after the hydrothermal process, the oxygen content obviously decreased from 1.05 to 0.49. Furthermore, a weak oxidation peak of O-P=O appeared at 133.0 eV in BRP. This could be ascribed to the partial re-oxidation of reactive BRP during the preparation process. FT-IR results showed no obvious change after the modification processes (Fig. 3e). Moreover, no characteristic peaks of EDA like C-N bond (1065 cm^{-1}) and N-H (1608 cm^{-1}) appeared after EDA treatment (Krishnan and Plane, 1966), corroborating the minor EDA amount in BRP.

3.3. Enhanced CBZ degradation performance

CBZ degradation experiments were carried out to evaluate the performance of pristine RP, HRP and BRP. As shown in Fig. 4a, all of them showed a weak direct activation ability towards PMS. Though Fe^{2+}/PMS alone could degrade 24.8% CBZ, this reaction almost terminated within 30 s. Besides, this two-stage kinetic bottleneck could not be mitigated even with higher Fe^{2+} or PMS dosage (Fig. S9). However, after the addition of RP, HRP and BRP, the two-stage kinetic bottleneck was greatly mitigated. Specifically, compared with the incomplete CBZ degradation by pristine RP, 100% CBZ degradation could be observed in 7.5 min by HRP. This confirmed that the size decrease effect and the removal of surface oxidation layer could greatly elevate the reducibility of RP. Moreover, complete CBZ depletion was observed even within 5 min using BRP. To exclude the influence of specific surface area, the BET normalized k_{obs} was calculated and it increased from 0.01 $g \bullet min^{-1} \bullet m^{-2}$ of HRP to 0.06 $g \bullet min^{-1} \bullet m^{-2}$ of BRP (Table S3). This

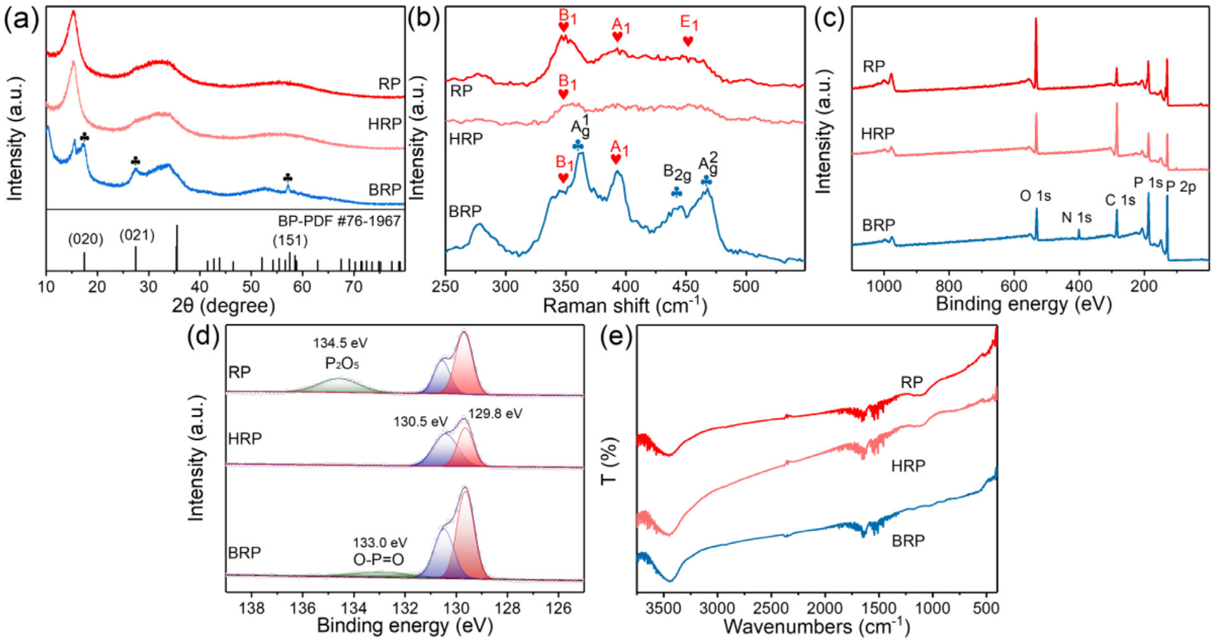

Fig. 3. (a) XRD patterns of pristine RP, HRP and BRP; (b) Raman spectra of RP, HRP and BRP; (c) XPS survey of RP, HRP and BRP; (d) P 2p core-level spectra of RP, HRP and BRP. (e) FT-IR spectra of RP, HRP and BRP.

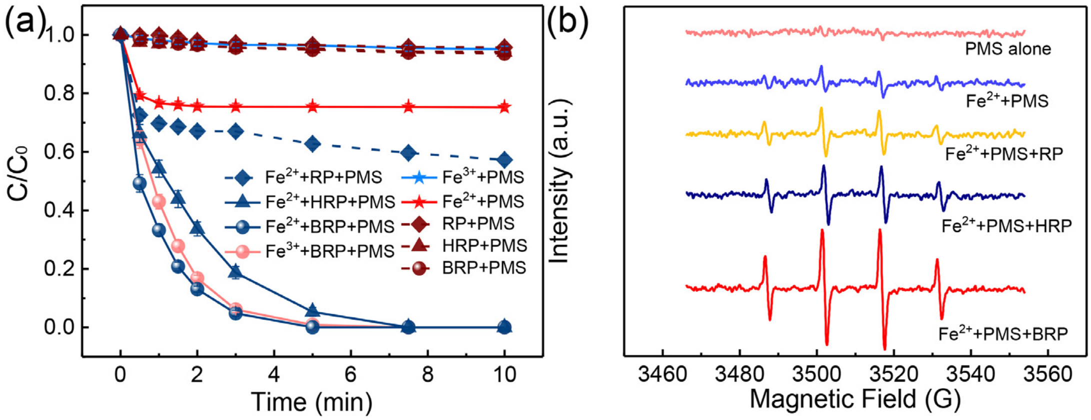

Fig. 4. (a) The performance of pristine RP, HRP and BRP in accelerating Fe^{3+}/Fe^{2+} cycle for PMS activation; (b) DMPO trapped EPR spectra of different systems. Experiment conditions: [RP] = [HRP] = [BRP] = 0.075 g/L, [PMS] = 0.2 mM, $[Fe^{3+}] = [Fe^{2+}]$ = 2 mg/L, $[CBZ]_0$ = 10.6 μM, [DMPO] = 10 mM, pH_{ini} = 3.0.

implied that apart from size decrease effect and oxidation layer removal, the role of partial phase conversion was also crucial in accelerating the electron transfer to regenerate Fe^{2+}.

According to the quenching experiments (Fig. S10), sulfate radicals ($SO_4^{\bullet-}$) and hydroxyl radicals (•OH) were identified as the reactive species in the system. $SO_4^{\bullet-}$ played a dominant role since the quenching effect of ethanol was more significant than that of tert butyl alcohol (Zhou et al., 2020). EPR results further demonstrated that the radical generation was most boosted in the order of BRP, HRP and pristine RP (Fig. 4b). The detected CBZ degradation intermediates and the possible degradation pathways were similar to other $SO_4^{\bullet-}$ dominated systems (more details in Text S4, Table S4 and Fig. S11) (Wu et al., 2020; Zhou et al., 2020). Acridone (ACON, *m/z* = 196.0755) was also the detected final products of CBZ. To investigate whether ACON, which is hard to be completely degraded through conventional treatment process (Kosjek et al., 2009), would accumulate in this system, the degradation of ACON was also conducted (Fig. S12). The results showed that though a little slower than CBZ, ACON would be still degraded in Fe^{3+}/PMS/BRP system, manifesting the minor accumulation of this hazardous intermediate.

To compare the intrinsic reducibility of RP, HRP and BRP, we first monitored the concentration of Fe^{2+} and residual PMS. Obviously, RP, HRP and BRP could directly reduce 0.18 mg/L, 1.24 mg/L and 1.57 mg/L Fe^{3+} in 20 min, respectively (Fig. 5a). Besides, these materials could not adsorb Fe^{2+}, suggesting the generated Fe^{2+} would not accumulate on the surfaces of these materials (Fig. S13). In the presence of PMS, the Fe^{2+} concentration remained low within 15 min due to the fast reaction between regenerated Fe^{2+} and PMS. After 15 min, it gradually rebounded owing to the depletion of PMS. This phenomenon was also consistent with previous studies using zero-valent metal or metal sulfides as the reductants (Sheng et al., 2019; Yi et al., 2019). The time profiles of PMS decomposition showed that 31.2% and 62.3% PMS could be directly consumed by HRP and BRP in 20 min due to their strong reducibility (Fig. 5b). With the addition of Fe^{3+}, PMS consumption rate ac-

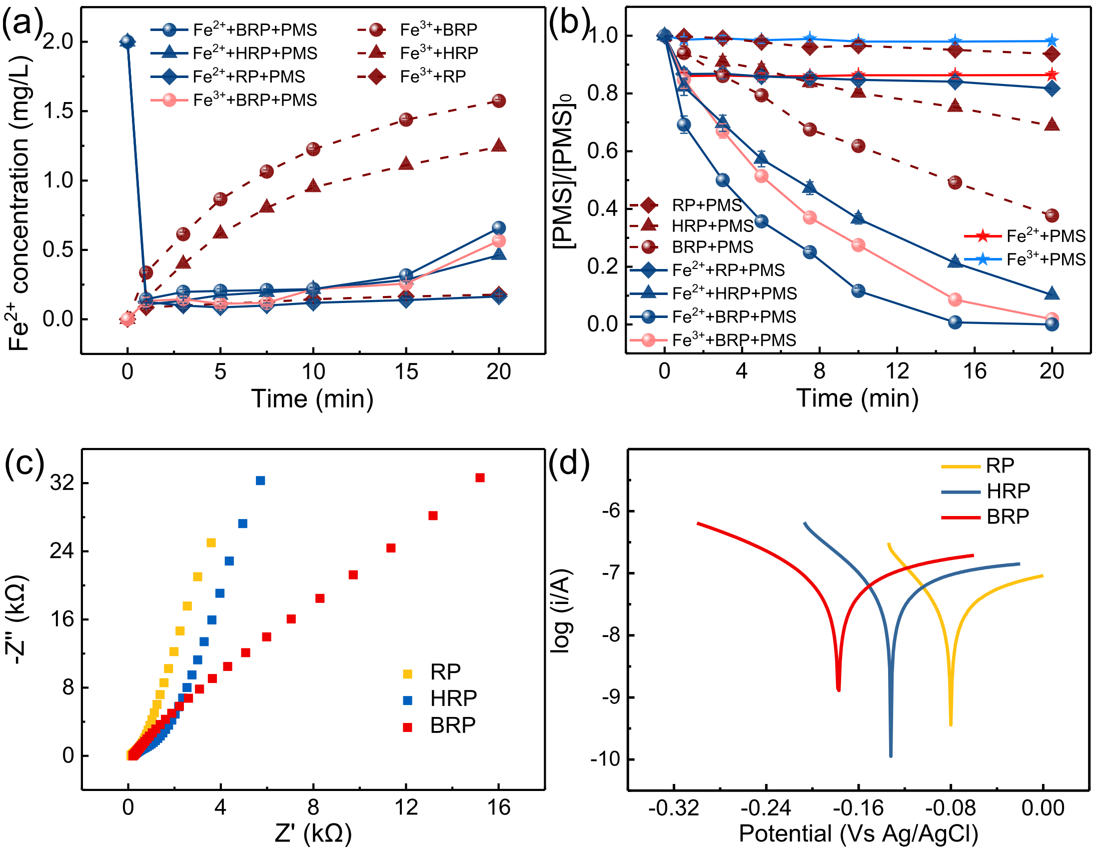

Fig. 5. (a) Time profiles of Fe^{2+} concentration in different systems; (b) Time profiles of residual PMS concentration in different systems; (c) Nyquist plots and (d) Tafel scans of pristine RP, HRP and BRP. Experiment conditions: [RP] = [HRP] = [BRP] = 0.075 g/L, [PMS] = 0.2 mM, $[Fe^{3+}] = [Fe^{2+}] = 2$ mg/L, $[CBZ]_0 = 10.6$ μM, $pH_{ini} = 3.0$.

celerated and most of the PMS could be depleted in 15 min. This implied that the addition of Fe^{3+} could promote the electron transfer from BRP to Fe^{3+} and further to PMS. Besdies, the enhanced electron transfer efficiency could be also reflected by the Nyquist plots and Tafel scans (Fig. 5c and d). The arc sizes of HRP and BRP were smaller than RP, indicating the higher electron conductivity of HRP and BRP than that of RP (Lim et al., 2019). Of note, the arc size of BRP in high frequency region was greater than that of HRP, which might be ascribed to the partial re-oxidation of BRP as shown in XPS spectra (Fig. 3d). However, despite a lower electron conductivity than HRP, the corrosion currents of RP, HRP and BRP calculated from the Tafel slope were 3.17×10^{-8}, 5.04×10^{-8} and 1.05×10^{-7} A, respectively. The higher corrosion current of BRP suggested that BRP was more liable to be corroded and donate electrons to oxidants during a redox reaction, which might be ascribed to the presence of more reactive BP phase.

3.4. Stability and broad applicability

To study the stability of BRP after the reaction, the reacted BRP was then characterized. From the SEM image, the BRP surface was corroded due to the oxidation by Fe^{3+} and PMS (Fig. S14). It could be also observed from the XRD pattern that the peak intensity declined after the reaction (Fig. S15a). Raman spectrum showed that the characteristic band of BP still existed, whereas the oxidation degree of BRP increased as the ratio of A_g^1 to A_g^2 declined from 1.56 to 0.94 (Fig. S15b) (Favron et al., 2015). P 2p core-level spectra confirmed the surface oxidation of BRP as well since the peak intensity of O-P=O at 133.0 eV decreased while the peak of P_2O_5 at 134.4 eV emerged again (Fig. S16). The atomic ratio of O to P also slightly increased to 0.57 after the reaction. However, the cyclic performance and Fe^{3+} reduction ability did not decline severely (Fig. 6a and Fig. S17). Even after five successive experiments, 100% CBZ could be still degraded. This suggested that the slight re-oxidation would not severely decrease the reactivity of BRP.

Furthermore, to investigate its applicability in various conditions, the influence of pH, dissolved O_2 and actual water was discussed. First, this system had a strong resistance to initial pH (3-6.1) due to the release of H^+ from PMS (Fig. S18). However, when buffered with acetic acid, the optimal pH was less than 5. This was because the increase of buffer pH would result in the hydrolysis of Fe^{3+}, which would be unfavorable for both the reduction of Fe^{3+} and the activation of PMS. Moreover, dissolved O_2 only showed a slight impact on CBZ degradation, revealing that this system was not sensitive to dissolved O_2 (Fig. 6b). More importantly, even in some actual water samples like tap water, Funan River, Jingcheng Lake and Yangtze River, 100% CBZ could be removed in 10 min, which exhibited its strong resistance to water matrix (Table S5 and Fig. 6c). Besides, the superior efficiency could be also reflected from the fast degradation of 9 typical contaminants including atrazine, levofloxacin, bisphenol-S, p-nitrophenol, 2,4-dichlorophenol, benzoic acid, bezafibrate, iohexol and diphenhydramine (Fig. S19). Furthermore, to confirm the broad applicability of BRP, the activation of H_2O_2 and PDS was also conducted (Fig. S20). 82.8% and 64.5% CBZ could be also effectively degraded with H_2O_2 and PDS respectively, which suggested the universality of BRP in catalytic organic oxidation. Finally, apart from orgaic degradation, BRP could be also applied in high-valent metal, like Cr (VI), reduction. Specifically, 86.3% Cr (VI) could be efficiently removed by 0.4 g/L BRP in 30 min, which indicated its strong reducibility (Fig. 6d).

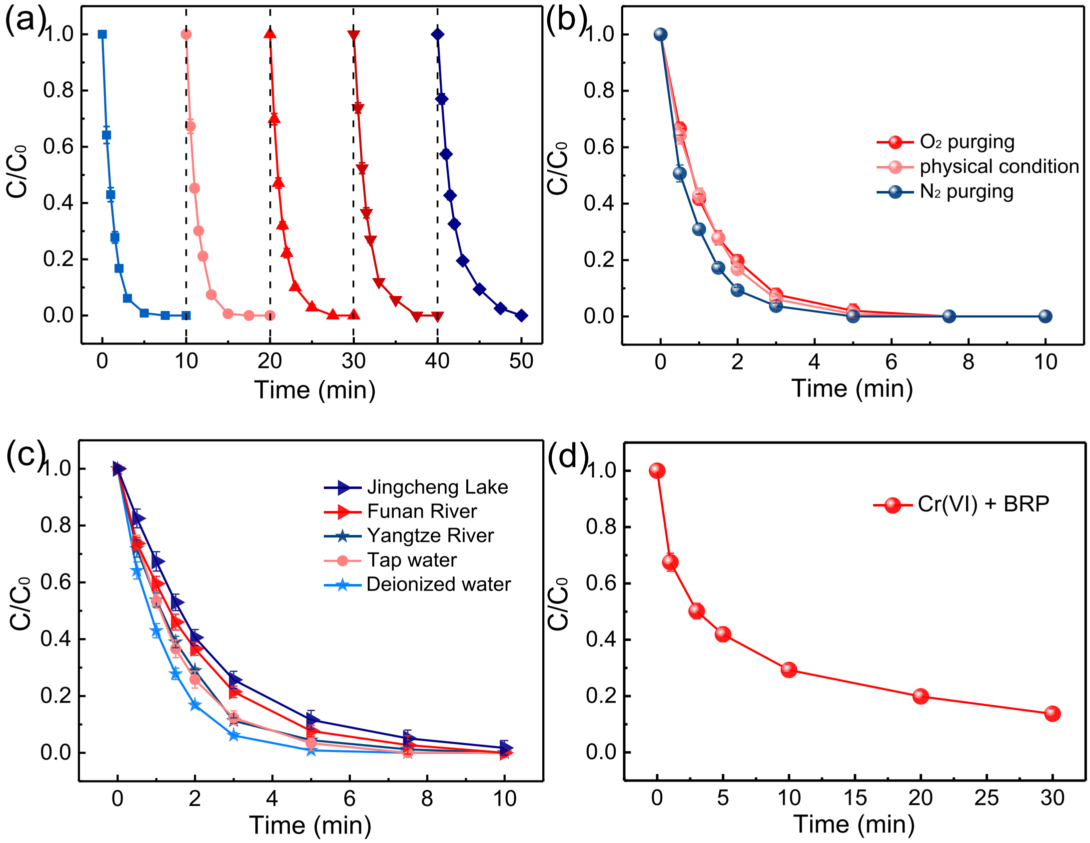

Fig. 6. (a) Cyclic performance of BRP in Fe^{3+}/PMS/BRP system; (b) The influence of different atmosphere on the CBZ degradation in Fe^{3+}/PMS/BRP system; (c) Performance of Fe^{3+}/PMS/BRP system in different actual water. Experiment conditions: [BRP] = [Five-cycle reacted BRP] = 0.075 g/L, [PMS] = 0.2 mM, $[Fe^{3+}]$ = 2 mg/L, $[CBZ]_0$ = 10.6 μM, pH_{ini} = 3.0. (d) Cr (VI) removal by BRP alone as a function of time. Experiment condition: [BRP] = 0.4 g/L, [Cr (VI)] = 10 mg/L, pH_{ini} = 3.0.

3.5. *The influence of reagent dosage and the mitigation of competition reaction*

To figure out the primary factors that determine the overall reaction kinetics, the influence of BRP dosage, Fe^{2+} dosage, PMS dosage and initial CBZ concentration was studied and analyzed in detail in Text S5, Fig. S21 and Fig. S22. From the analysis results, the influence of BRP dosage, Fe^{2+} dosage and initial CBZ concentration on the degradation efficiency and the corresponding k_{obs} was primary, whereas the influence of PMS dosage was minor. According to Fig. 5a, the transient Fe^{2+} concentration during 15 min was low. Therefore, the initial PMS dosage was relatively excessive compared with Fe^{2+} concentration. Even with a high PMS dosage, the reaction rate would not obviously increase. Besides, the excessive PMS present in the system would be also ineffectively consumed by reductive BRP without CBZ degradation (Fig. 5b). Herein, to alleviate this competition reaction, multiple dosage was conducted since multiple dosage could avoid the unnecessary interaction between BRP and PMS. A higher CBZ concentration was used to evaluate the overall PMS utilization efficiency. Besdies, the total PMS and BRP dosages were kept constant to compare the final CBZ degradation efficiency.

As shown in Fig. 7a, the degradation efficiency after 30 min increased from 64.8% to 78.4% and 80.7% with twice and four-time PMS dosage, respectively. This confirmed that multiple PMS dosage could actually alleviate the side reaction between PMS and BRP and reduce PMS consumption, thus promoting more radical generation. Conversely, multiple BRP dosage hampered CBZ degradation (Fig. 7b). Though multiple BRP dosage could also alleviate the side reaction, the reduction of Fe^{3+} by BRP was also slowed down. Herein, multiple BRP dosage was unfavourable for the overall CBZ degradation efficiency.

To comprehend the behavior of BRP thoroughly, the influence of multiple dosage on the performance of two benchmark reductants (based on substantial previous works, Table S6), i.e. homogeneous NH_2OH and heterogeneous MoS_2, was also investigated. From Fig. 7c and e, multiple PMS dosage was less effective for MoS_2 and NH_2OH. This could be ascribed to their relatively slow direct reaction with PMS, which would not cause prompt PMS consumption (Sheng et al., 2019; Zou et al., 2013). Similar to BRP, multiple MoS_2 and NH_2OH dosage could not promote CBZ degradation either, which was due to the slower Fe^{3+} reduction rate (Fig. 7d and f) (Li et al., 2020). The intrinsic reducibility of NH_2OH, MoS_2 and BRP was also compared via Fe^{2+} generation amount (Fig. S23). The result showed that homogeneous NH_2OH quickly reduced Fe^{3+} within 1 min, whereas heterogeneous BRP and MoS_2 gradually generated Fe^{2+}. Though the Fe^{3+} reduction reaction by NH_2OH proceeded promptly, the final CBZ degradation efficiency was only ~50% no matter which dosage mode was conducted. This indicated that the quenching effects between NH_2OH and radicals in homogeneous solution were inevitable (Zou et al., 2013). However, the final CBZ degradation efficiencies were 64.8% and 69.1% for BRP and MoS_2, respectively. This suggested the superiority of heterogeneous reductants in avoiding radical quenching by reductants themselves. Although the side reaction would hamper the performance of BRP compared with MoS_2, multiple BRP dosage could significantly alleviate the side reaction and promote CBZ degradation to 80.7%. Thus, with less radical quenching than hydroxylamine and stronger reducibility than MoS_2, BRP exhibited a great potential as Fe^{3+} reductant in PMS activation.

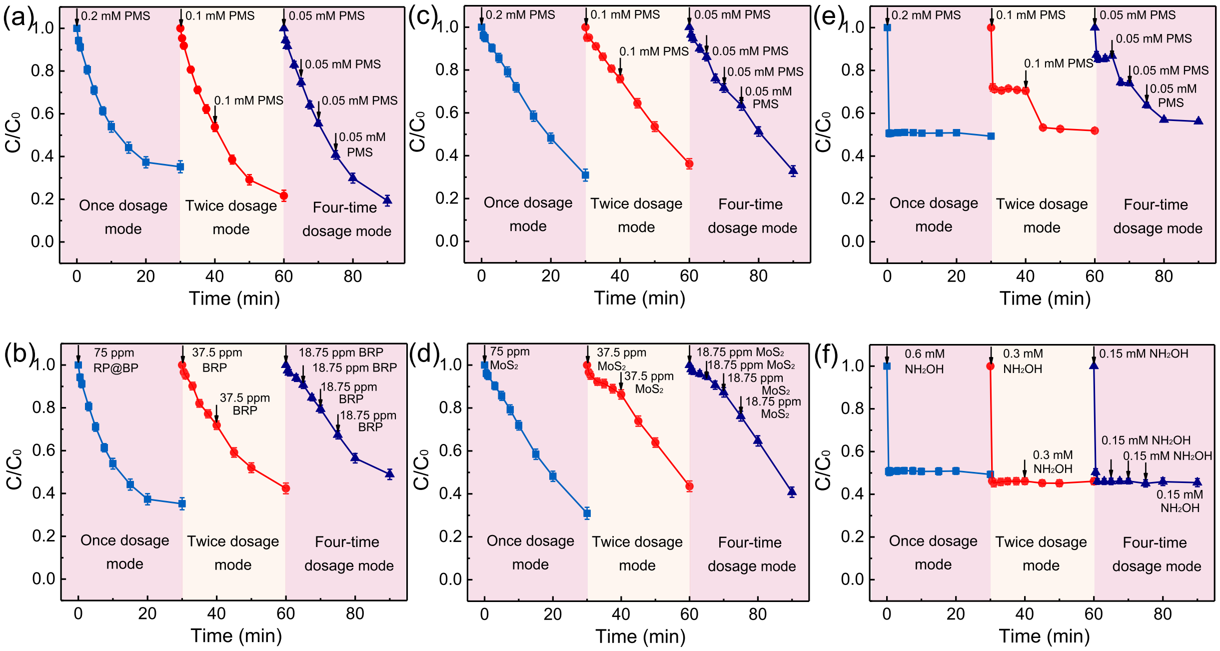

Fig. 7. The influence of (a) PMS and (b) BRP dosage mode on high-concentration CBZ degradation in Fe^{3+}/PMS/BRP system; The influence of (c) PMS and (d) MoS_2 dosage mode on high-concentration CBZ degradation in Fe^{3+}/PMS/MoS_2 system; The influence of (e) PMS and (f) NH_2OH dosage mode on high-concentration CBZ degradation in Fe^{3+}/PMS/NH_2OH system. Experiment conditions: [BRP] = [MoS_2] = 0.075 g/L, [NH_2OH] = 0.6 mM, [PMS] = 0.2 mM, [Fe^{3+}] = 2 mg/L, $[CBZ]_0$ = 84.7 μM, pH_{ini} = 3.0.

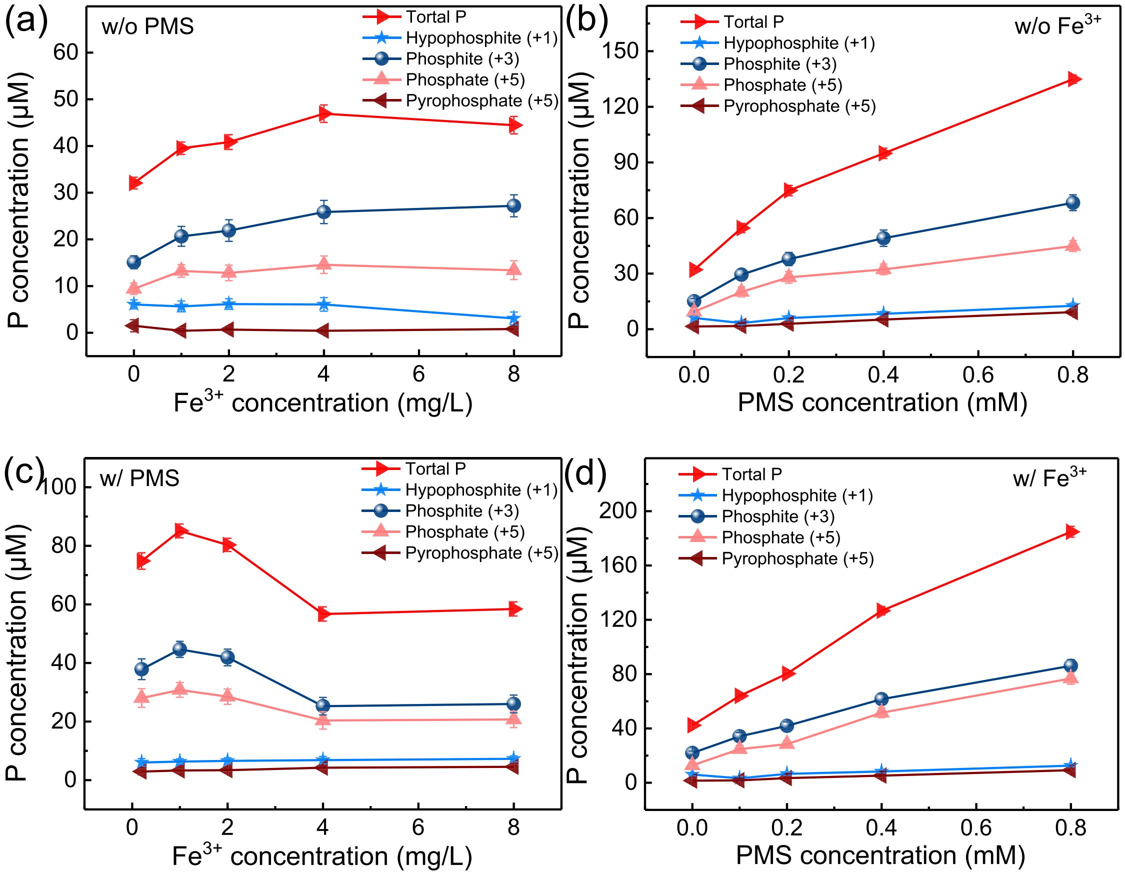

Fig. 8. BRP oxidation product generation by (a) Fe^{3+} alone; (b) PMS alone; (c) PMS with different Fe^{3+} concentration and (d) Fe^{3+} with different PMS concentration. Experiment condition: [BRP] = 0.075 g/L, [Fe^{3+}] = 2 mg/L, [PMS] = 0.2 mM, $[CBZ]_0$ = 10.6 μM, pH_{ini} = 3.0, reaction time = 20 min.

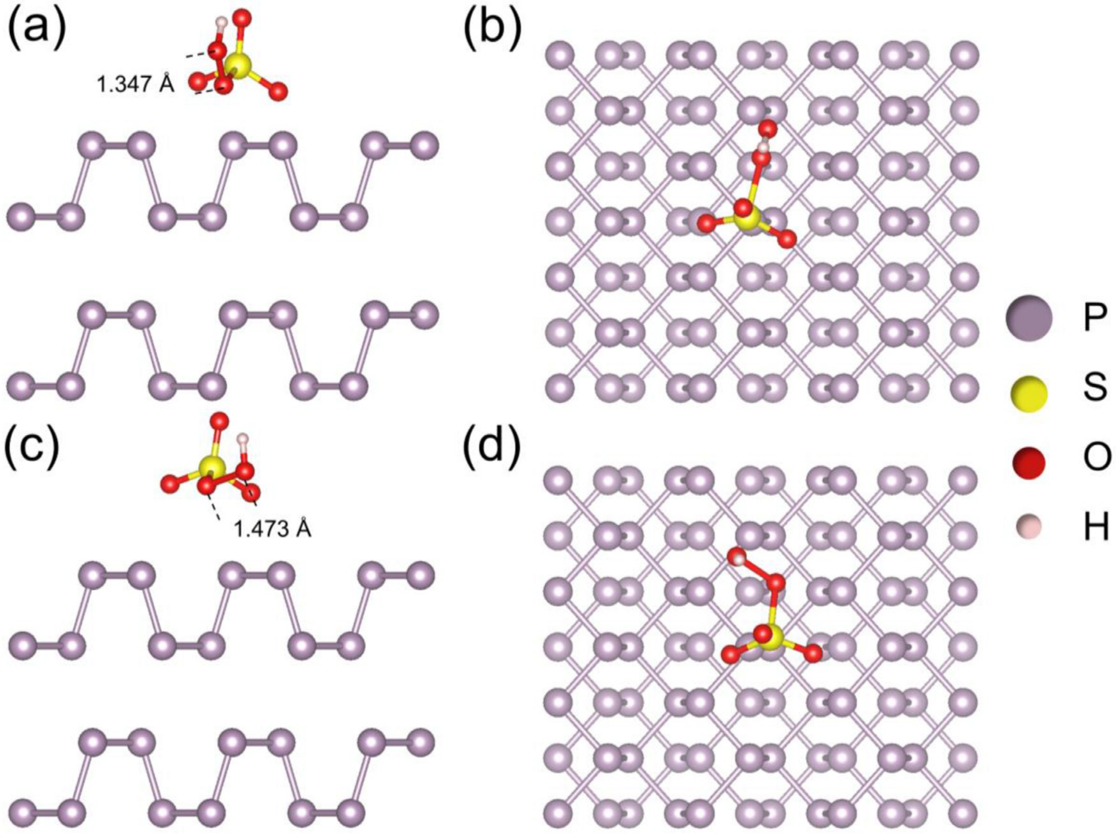

Fig. 9. (a) Side view and (b) top view of the PMS adsorption model before optimization; (c) Side view and (d) top view of the PMS adsorption model after optimization.

3.6. Phosphorus by-product formation and corresponding control strategy

As a reductant, BRP would proceed self-transformation and generate various phosphorus by-products such as hypophosphite (+1), phosphite (+3), phosphate (+5) and pyrophosphate (+5) (Zhang et al., 2019c). To control the phosphorus by-product formation, it was of vital importance to get insights into their formation mechanism. Thus, we utilized ion chromatography to investigate by-product formation under various conditions. Fig. S24 depicted the time profiles of different phosphorus by-product formation in Fe^{3+}/PMS/BRP system. Obviously, phosphite and phosphate were the primary phosphorus intermediates, while hypophosphite and pyrophosphate only accounted for a small proportion. Fig. 8a further depicted the oxidation of BRP by Fe^{3+} alone. With the increase of Fe^{3+} dosage, the phosphite and phosphate concentration gradually ascended to 27 μM and 13.5 μM, respectively. Although hypophosphite and phosphite were reported to be moderate reductants (Feng et al., 2018), they could not reduce Fe^{3+} and accelerate CBZ degradation under our experimental conditions (Fig. S25). Herein, the reduction of Fe^{3+} was primarily a surface reaction.

Compared with Fe^{3+}, the contribution of PMS to P by-product generation was more remarkable (Fig. 8b). The concentration of phosphite and phosphate significantly ascended to 68 μM and 44.8 μM, while hypophosphite and pyrophosphate gradually ascended to 12.6 μM and 9.4 μM as PMS dosage increased to 0.8 mM. Of note, though hypophosphite could be partially oxidized to phosphite by PMS alone through an oxygen transfer reaction (Dubey et al., 2002), phosphite was less oxidized to phosphate by PMS alone (Fig. S26). Therefore, the formation of phosphorus products dominantly derived from the surface BRP oxidation by PMS. Given the minor CBZ degradation efficiency in PMS/BRP alone system (Fig. 4a), the one-electron transfer pathway of PMS generating radicals could be excluded (Gábor et al., 2009). Based on the above facts, a plausible reaction mechanism could be proposed that PMS mainly oxidized BRP through a two-electron transfer pathway without radcial generation. Specifically, PMS could first oxidize BRP through a two-electron reaction with minor surface P (0) disproportionating into hypophosphite (+1) and phophite (+3). Then the residual surface P would be further oxidized through another two-electron transfer reaction and disproportionate into phosphite (+3) and phosphate (+5, or pyrophosphate). Incidentally, the concentration of phosphite approximately equalled the sum of the concentration of hypophosphite, phosphate and pyrophosphate, which also substantiated this mechanism (Eq. (6), Fig. S27).

$$[P]_{\text{phosphite}\,(+3)} \approx [P]_{\text{hypophosphite}\,(+1)} + [P]_{\text{phosphate}\,(+5)} + [P]_{\text{pyrophosphate}\,(+5)} \tag{6}$$

Moreover, the reaction between BRP and PMS was also simulated via DFT calculation. Given that the structure of amorphous RP is still under dispute (Zhang et al., 2019b), the calculation model was established using the BP phase to investigate their interaction preliminarily. From Fig. 9, it could be found that PMS was mainly adsorbed at the H site above the P_6 hexagon of BP surface (Kulish et al., 2015). The adsorption energy was calculated as -1.18 eV, implying the reaction between BRP and PMS could proceed spontaneously. The charge density difference illustrated an obvious charge accumulation in PMS and charge depletion in BP (Fig. S28).

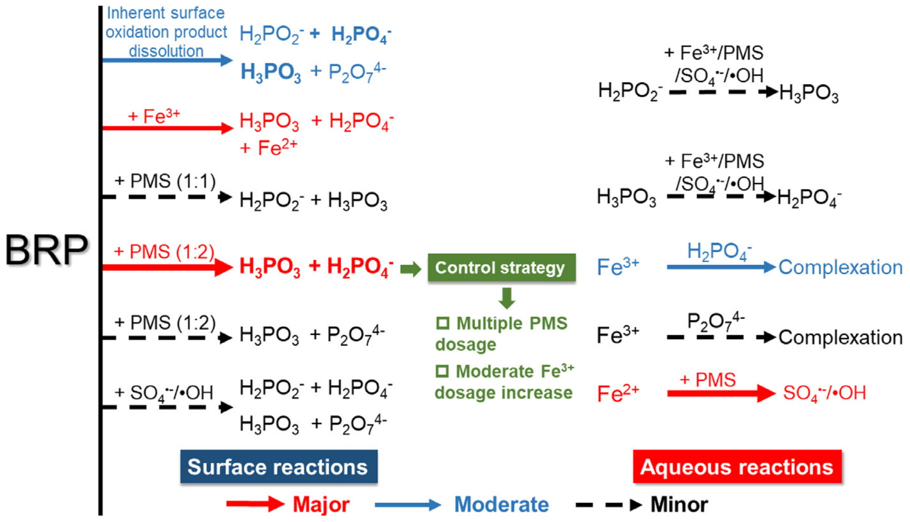

Scheme 1. Reaction mechanism of Fe^{3+}/PMS/BRP system.

Besides, the O-O bond length also increased from 1.347 Å to 1.473 Å, suggesting the cleavage tendency of O-O bond. Overall, strong electron transfer would occur between BRP and PMS, which might lead to the unnecessary consumption of PMS.

Furthermore, the influence of Fe^{3+} on BRP oxidation in the presence of PMS and the influence of PMS on BRP oxidation in the presence of Fe^{3+} were studied. In Fig. 8c, the phosphite, phosphate and total P concentration first ascended a little at small Fe^{3+} dosage but then gradually descended at higher Fe^{3+} dosage. The initial minor increase could be ascribed to the faster and more PMS decomposition compared with no Fe^{3+} addition (Fig. 5b). Then as the Fe^{3+} concentration increased, more Fe^{2+} could be generated which could effectively utilize PMS and thus inhibit the undesirable side-reaction between BRP and PMS. Of note, the oxidation of BRP by $SO_4^{\bullet-}$ and •OH should be marginal since the P intermediate generation decreased when more radicals were generated with more Fe^{3+} dosage. In contrast, increasing the PMS concentration with a fixed amount of Fe^{3+} even resulted in more P oxidation product generation than PMS alone (Fig. 8d). This could be also ascribed to the faster and more PMS decomposition in the presence of Fe^{3+}. All these confirmed that adequate Fe^{2+} formation was conducive to mitigating P by-product formation and elevating PMS utilization efficiency.

Moreover, the influence of these P oxidation products on CBZ degradation efficiency was further studied (Fig. S29). The four P oxidation products were disadvantageous to the CBZ degradation and the degradation efficiency declined in the order of phosphite, hypophosphite, phosphate and pyrophosphate. The secondary reaction rate constants *k* of $SO_4^{\bullet-}$ and •OH with these anions, PMS and CBZ were listed in Table S7 and the corresponding *ck* values were calculated (Table S8). Although the *ck* value of •OH with CBZ is lower than those with hypophosphite and phosphite, the *ck* values of $SO_4^{\bullet-}$ with CBZ is comparable to those with hypophosphite and phosphite. Thus, in view of the more $SO_4^{\bullet-}$ generation in this system, the influence of hypophosphite and phosphite on CBZ degradation should be minor. As for phosphate and pyrophosphate, despite the lower *ck* values, they could otherwise complex with Fe^{3+} and thus retard Fe^{3+} reduction. Nevertheless, given the small amount of these anions, the actual inhibition effects were marginal.

Finally, according to the above discussion, all the reactions in Fe^{3+}/PMS/BRP system were illustrated in Scheme 1. Obviously, the competition reaction between PMS and BRP mainly contributed to phosphorus by-product formation. Therefore, an appropriate initial Fe^{3+} concentration and a multiple PMS dosage might be essential to inhibit phosphorus by-product generation and promote target contaminant degradation. However, despite these strategies, a part of phosphite and phosphate could still remain in the effluent. Phosphate could be removed via precipitation process, while phosphite might require an extra step to remove. To efficiently solve this problem and reduce the treatment costs, some newly-emerging techniques like capacitive deionization could be investigated in the future. Nevertheless, compared with other oxidation system using polyphosphate as the ligand (Kim et al., 2015; Zong et al., 2020) or Cu_xP as the reagents (Kim et al., 2019), the phosphorus generation stress in this system was minor, suggesting its great potential in organic oxidation.

4. Conclusion

In this work, we developed a metal-free heterogenous reductant to accelerate Fe^{3+}/Fe^{2+} cycle for PMS activation. We found that after two-step modification, the obtained BRP possessed a greater BET surface area with a less oxidation layer and partially converted to BP phase. All these aspects contributed to the enhanced electron transfer capacity from BRP to Fe^{3+}. Besides, BRP exhibited an excellent recyclability and strong resistance to dissolved oxygen and water matrix. As a heterogeneous reductant, BRP avoided the quenching reaction with radicals which was inevitable when using homogeneous reductants. Though undesirable competition reaction between PMS and BRP would occur, multiple PMS dosage could remarkedly alleviate the competetion reaction and elevate PMS utilization efficiency. The dominant BRP oxidation products included phosphite and phosphate, which mainly derived from the surface two-electron reaction between PMS and BRP. Interestingly, moderate increase of Fe^{3+} dosage could efficiently reduce by-product generation via the prompt PMS activation by regenerated Fe^{2+}. Hence, with a comparable efficiency for promoting Fe^{3+}/Fe^{2+} cycle, the emergence of metal-free and environment-benign BRP could avoid the use of heavy-metal-bearing materials or toxic hydroxylamine. We believe this work would promote the application of non-metallic elements in reductant-involved environmental remediation.

Declaration of Competing Interest

The authors declare that they have no known competing financial interests or personal relationships that could have appeared to influence the work reported in this paper.

Acknowledgment

The authors would like to acknowledge the financial support from National Natural Science Foundation of China, China (no. 51878423), Sichuan science and technology program: key research and development program (no. 2019YFG0314, no. 2017SZ0180, no. 2019YFG0324). The authors would like to thank the Analytical & Testing Center of Sichuan University for EPR detection and thanks to Dr. Hanjiao Chen for his assistance with the EPR analyses.

Supplementary materials

Supplementary material associated with this article can be found, in the online version, at doi:10.1016/j.watres.2020.116529.

References

Andreozzi, R., Canterino, M., Marotta, R., 2006. Fe(III) homogeneous photocatalysis for the removal of 1,2-dichlorobenzene in aqueous solution by means UV lamp and solar light. Water Res. 40 (20), 3785–3792.

Anipsitakis, G.P., Dionysiou, D.D., 2004. Radical generation by the interaction of transition metals with common oxidants. Environ. Sci. Technol. 38 (13), 3705–3712.

Antonatos, N., Bouša, D., Kovalska, E., Sedmidubský, D., Růžička, K., Vrbka, P., Veselý, M., Hejtmánek, J., Sofer, Z., 2020. Large-scale production of nanocrystalline black phosphorus ceramics. ACS Appl. Mater. Interfaces 12 (6), 7381–7391.

Apul, O.G., Karanfil, T., 2015. Adsorption of synthetic organic contaminants by carbon nanotubes: a critical review. Water Res. 68, 34–55.

Batmunkh, M., Myekhlai, M., Bati, A.S.R., Sahlos, S., Slattery, A.D., Benedetti, Tania M., Gonçales, V.R., Gibson, C.T., Gooding, J.J., Tilley, R.D., Shapter, J.G., 2019. Microwave-assisted synthesis of black phosphorus quantum dots: efficient electrocatalyst for oxygen evolution reaction. J. Mater. Chem. A 7 (21), 12974–12978.

Brillas, E., Sirés, I., Oturan, M.A., 2009. Electro-Fenton process and related electrochemical technologies based on Fenton's reaction chemistry. Chem. Rev. 109 (12), 6570–6631.

Cartz, L., Srinivasa, S.R., Riedner, R.J., Jorgensen, J.D., Worlton, T.G., 1979. Effect of pressure on bonding in black phosphorus. J. Chem. Phys. 71 (4), 1718–1721.

Duan, X., Li, W., Ao, Z., Kang, J., Tian, W., Zhang, H., Ho, S.-H., Sun, H., Wang, S., 2019. Origins of boron catalysis in peroxymonosulfate activation and advanced oxidation. J. Mater. Chem. A 7 (41), 23904–23913.

Dubey, S., Hemkar, S., Khandelwal, C.L., Sharma, P.D., 2002. Kinetics and mechanism of oxidation of hypophosphorous acid by peroxomonosulphate in acid aqueous medium. Inorg. Chem. Commun. 5 (10), 903–908.

Favron, A., Gaufrès, E., Fossard, F., Phaneuf-L'Heureux, A.-L., Tang, N.Y.W., Lévesque, P.L., Loiseau, A., Leonelli, R., Francoeur, S., Martel, R., 2015. Photooxidation and quantum confinement effects in exfoliated black phosphorus. Nat. Mater. 14, 826.

Feng, M., Jinadatha, C., McDonald, T.J., Sharma, V.K., 2018. Accelerated oxidation of organic contaminants by ferrate(VI): the overlooked role of reducing additives. Environ. Sci. Technol. 52 (19), 11319–11327.

Fukuchi, S., Nishimoto, R., Fukushima, M., Zhu, Q., 2014. Effects of reducing agents on the degradation of 2,4,6-tribromophenol in a heterogeneous Fenton-like system with an iron-loaded natural zeolite. Appl. Catal. B Environ. 147, 411–419.

Gábor, L., József, K., Zsuzsa, B., Alíz, K., Ildikó, K., Dávid, B., Marcell, T., Lilla, V., István, F., 2009. One- versus two-electron oxidation with peroxomonosulfate ion: reactions with iron(II), vanadium(IV), halide ions, and photoreaction with cerium(III). Inorg. Chem. 48 (4), 1763–1773.

He, D., Cheng, Y., Zeng, Y., Luo, H., Luo, K., Li, J., Pan, X., Barceló, D., Crittenden, J.C., 2020. Synergistic activation of peroxymonosulfate and persulfate by ferrous ion and molybdenum disulfide for pollutant degradation: theoretical and experimental studies. Chemosphere 240, 124979.

Kim, H.-H., Lee, H., Kim, H.-E., Seo, J., Hong, S.W., Lee, J.-Y., Lee, C., 2015. Polyphosphate-enhanced production of reactive oxidants by nanoparticulate zero-valent iron and ferrous ion in the presence of oxygen: yield and nature of oxidants. Water Res. 86, 66–73.

Kim, H., Lim, J., Lee, S., Kim, H.-H., Lee, C., Lee, J., Choi, W., 2019. Spontaneous generation of H_2O_2 and hydroxyl radical through O_2 reduction on copper phosphide under ambient aqueous condition. Environ. Sci. Technol. 53 (5), 2918–2925.

Kosjek, T., Andersen, H.R., Kompare, B., Ledin, A., Heath, E., 2009. Fate of carbamazepine during water treatment. Environ. Sci. Technol. 43 (16), 6256–6261.

Kresse, G., Joubert, D., 1999. From ultrasoft pseudopotentials to the projector augmented-wave method. Phys. Rev. B 59 (3), 1758–1775.

Krishnan, K., Plane, R.A., 1966. Raman and infrared spectra of complexes of ethylenediamine with zinc(II), cadmium(II), and mercury(II). Inorg. Chem. 5 (5), 852–857.

Kulish, V.V., Malyi, O.I., Persson, C., Wu, P., 2015. Adsorption of metal adatoms on single-layer phosphorene. Phys. Chem. Chem. Phys. 17 (2), 992–1000.

Lee, H., Lee, H.-J., Seo, J., Kim, H.-E., Shin, Y.K., Kim, J.-H., Lee, C., 2016. Activation of oxygen and hydrogen peroxide by copper(II) coupled with hydroxylamine for oxidation of organic contaminants. Environ. Sci. Technol. 50 (15), 8231–8238.

Li, J., Wan, Y., Li, Y., Yao, G., Lai, B., 2019. Surface Fe(III)/Fe(II) cycle promoted the degradation of atrazine by peroxymonosulfate activation in the presence of hydroxylamine. Appl. Catal. B Environ. 256, 117782.

Li, T., Zhao, Z., Wang, Q., Xie, P., Ma, J., 2016. Strongly enhanced Fenton degradation of organic pollutants by cysteine: an aliphatic amino acid accelerator outweighs hydroquinone analogues. Water Res. 105, 479–486.

Li, Z.-Y., Wang, L., Liu, Y.-L., Zhao, Q., Ma, J., 2020. Unraveling the interaction of hydroxylamine and Fe(III) in Fe(II)/Persulfate system: a kinetic and simulating study. Water Res. 168, 115093.

Lim, J., Lee, J.M., Kim, C., Hwang, S.-J., Lee, J., Choi, W., 2019. Two-dimensional RuO_2 nanosheets as robust catalysts for peroxymonosulfate activation. Environ. Sci.: Nano 6 (7), 2084–2093.

Liu, F., Shi, R., Wang, Z., Weng, Y., Che, C.-M., Chen, Y., 2019. Direct Z-scheme hetero-phase junction of black/red phosphorus for photocatalytic water splitting. Angew. Chem. Int. Ed. 58 (34), 11791–11795.

Liu, J., Dong, C., Deng, Y., Ji, J., Bao, S., Chen, C., Shen, B., Zhang, J., Xing, M., 2018a. Molybdenum sulfide Co-catalytic Fenton reaction for rapid and efficient inactivation of *Escherichia coli*. Water Res. 145, 312–320.

Liu, R., Zhao, H., Zhao, X., He, Z., Lai, Y., Shan, W., Bekana, D., Li, G., Liu, J., 2018b. Defect sites in ultrathin Pd nanowires facilitate the highly efficient electrochemical hydrodechlorination of pollutants by H^*ads. Environ. Sci. Technol. 52 (17), 9992–10002.

Nie, C., Dai, Z., Liu, W., Duan, X., Wang, C., Lai, B., Ao, Z., Wang, S., An, T., 2020. Criteria of active sites in nonradical persulfate activation process from integrated experimental and theoretical investigations: boron–nitrogen-Co-doped nanocarbon-mediated peroxydisulfate activation as an example. Environ. Sci.: Nano 7 (7), 1899–1911.

Nie, C., Dai, Z., Meng, H., Duan, X., Qin, Y., Zhou, Y., Ao, Z., Wang, S., An, T., 2019. Peroxydisulfate activation by positively polarized carbocatalyst for enhanced removal of aqueous organic pollutants. Water Res. 166, 115043.

Pignatello, J.J., Oliveros, E., MacKay, A., 2006. Advanced oxidation processes for organic contaminant destruction based on the Fenton reaction and related chemistry. Cri. Rev. Environ. Sci. Technol. 36 (1), 1–84.

Rastogi, A., Al-Abed, S.R., Dionysiou, D.D., 2009. Effect of inorganic, synthetic and naturally occurring chelating agents on Fe(II) mediated advanced oxidation of chlorophenols. Water Res. 43 (3), 684–694.

Seo, J., Lee, H.-J., Lee, H., Kim, H.-E., Lee, J.-Y., Kim, H.S., Lee, C., 2015. Enhanced production of reactive oxidants by Fenton-like reactions in the presence of carbon materials. Chem. Eng. J. 273, 502–508.

Shen, Z., Sun, S., Wang, W., Liu, J., Liu, Z., Yu, J.C., 2015. A black–red phosphorus heterostructure for efficient visible-light-driven photocatalysis. J. Mater. Chem. A 3 (7), 3285–3288.

Sheng, B., Yang, F., Wang, Y., Wang, Z., Li, Q., Guo, Y., Lou, X., Liu, J., 2019. Pivotal roles of MoS_2 in boosting catalytic degradation of aqueous organic pollutants by Fe(II)/PMS. Chem. Eng. J. 375, 121989.

Soufan, M., Deborde, M., Delmont, A., Legube, B., 2013. Aqueous chlorination of carbamazepine: kinetic study and transformation product identification. Water Res. 47 (14), 5076–5087.

Tian, B., Tian, B., Smith, B., Scott, M.C., Lei, Q., Hua, R., Tian, Y., Liu, Y., 2018. Facile bottom-up synthesis of partially oxidized black phosphorus nanosheets as metal-free photocatalyst for hydrogen evolution. Proc. Natl. Acad. Sci. USA 115 (17), 4345.

Wang, Y., Ma, W., Chen, C., Hu, X., Zhao, J., Yu, J.C., 2007. Fe^{3+}/Fe^{2+} cycling promoted by Ta_3N_5 under visible irradiation in Fenton degradation of organic pollutants. Appl. Catal. B Environ. 75 (3), 256–263.

Wu, Z., Wang, Y., Xiong, Z., Ao, Z., Pu, S., Yao, G., Lai, B., 2020. Core-shell magnetic Fe_3O_4@Zn/Co-ZIFs to activate peroxymonosulfate for highly efficient degradation of carbamazepine. Appl. Catal. B Environ. 277, 119136.

Xia, D., Shen, Z., Huang, G., Wang, W., Yu, J.C., Wong, P.K., 2015. Red phosphorus: an earth-abundant elemental photocatalyst for "green" bacterial inactivation under visible light. Environ. Sci. Technol. 49 (10), 6264–6273.

Xiao, S., Cheng, M., Zhong, H., Liu, Z., Liu, Y., Yang, X., Liang, Q., 2020. Iron-mediated activation of persulfate and peroxymonosulfate in both homogeneous and heterogeneous ways: a review. Chem. Eng. J. 384, 123265.

Xing, M., Xu, W., Dong, C., Bai, Y., Zeng, J., Zhou, Y., Zhang, J., Yin, Y., 2018. Metal sulfides as excellent Co-catalysts for H_2O_2 decomposition in advanced oxidation processes. Chem 4 (6), 1359–1372.

Yi, Q., Ji, J., Shen, B., Dong, C., Liu, J., Zhang, J., Xing, M., 2019. Singlet oxygen triggered by superoxide radicals in a molybdenum cocatalytic Fenton reaction with enhanced redox activity in the environment. Environ. Sci. Technol. 53 (16), 9725–9733.

You, J., Sun, W., Su, S., Ao, Z., Liu, C., Yao, G., Lai, B., 2020. Degradation of bisphenol A by peroxymonosulfate activated with oxygen vacancy modified nano-NiO-ZnO composite oxides: a typical surface-bound radical system. Chem. Eng. J. 400, 125915. doi:10.1016/j.cej.2020.125915.

Zhang, H., Ji, Q., Lai, L., Yao, G., Lai, B., 2019a. Degradation of p-nitrophenol (PNP) in aqueous solution by mFe/Cu-air-PS system. Chin. Chem. Lett. 30 (5), 1129–1132.

Zhang, S., Qian, H.-j., Liu, Z., Ju, H., Lu, Z.-y., Zhang, H., Chi, L., Cui, S., 2019b. Towards unveiling the exact molecular structure of amorphous red phosphorus by single-molecule studies. Angew. Chem. Int. Ed. 58 (6), 1659–1663.

Zhang, S., Zhang, X., Lei, L., Yu, X.-F., Chen, J., Ma, C., Wu, F., Zhao, Q., Xing, B., 2019c. pH-dependent degradation of layered black phosphorus: essential role of hydroxide ions. Angew. Chem. Int. Ed. 58 (2), 467–471.

Zhou, H., Lai, L., Wan, Y., He, Y., Yao, G., Lai, B., 2020. Molybdenum disulfide (MoS2): a versatile activator of both peroxymonosulfate and persulfate for the degradation of carbamazepine. Chem. Eng. J. 384, 123264.

Zong, Y., Mao, Y., Xu, L., Wu, D., 2020. Non-selective degradation of organic pollutants via dioxygen activation induced by Fe(II)-tetrapolyphosphate complexes: identification of reactive oxidant and kinetic modeling. Chem. Eng. J. 398, 125603.

Zou, J., Ma, J., Chen, L., Li, X., Guan, Y., Xie, P., Pan, C., 2013. Rapid acceleration of ferrous iron/peroxymonosulfate oxidation of organic pollutants by promoting Fe(III)/Fe(II) cycle with hydroxylamine. Environ. Sci. Technol. 47 (20), 11685–11691.